Quantum phase diagram of the two-dimensional transverse-field Ising model: Unconstrained tree tensor network and mapping analysis

M. Sadrzadeh,[1] R. Haghshenas,[2] and A. Langari[1,*]

[1]*Department of Physics, Sharif University of Technology, P.O. Box 11155-9161 Tehran, Iran*

[2]*Department of Physics and Astronomy, California State University, Northridge, California 91330, USA*

(Received 1 January 2019; revised manuscript received 31 March 2019; published 16 April 2019)

We investigate the ground-state phase diagram of the frustrated transverse-field Ising (TFI) model on the checkerboard lattice (CL), which consists of Néel, collinear, quantum paramagnet, and plaquette-valence bond solid (-VBS) phases. We implement a numerical simulation that is based on the recently developed unconstrained tree tensor network ansatz, which systematically improves the accuracy over the conventional methods as it exploits the internal gauge selections. At the highly frustrated region ($J_2 = J_1$), we observe a second-order phase transition from the plaquette-VBS state to the paramagnet phase at the critical magnetic-field $\Gamma_c = 0.28$ with the associated critical exponents $\nu = 1$ and $\gamma \simeq 0.4$, which are obtained within the finite-size scaling analysis on different lattice sizes $N = 4 \times 4, 6 \times 6, 8 \times 8$. The stability of the plaquette-VBS phase at low magnetic fields is examined by a spin-spin correlation function, which verifies the presence of plaquette-VBS at $J_2 = J_1$ and rules out the existence of a Néel phase. In addition, our numerical results suggest that the transition from the Néel (for $J_2 < J_1$) to the plaquette-VBS phase is a deconfined phase transition. Moreover, we introduce a mapping, which renders the low-energy effective theory of the TFI on the CL to be the same model on the $J_1 - J_2$ square lattice (SL). We show that the plaquette-VBS phase of the highly frustrated point $J_2 = J_1$ on the CL is mapped to the emergent string-VBS phase on the SL at $J_2 = 0.5J_1$.

DOI: 10.1103/PhysRevB.99.144414

I. INTRODUCTION

Quantum phases of matter without magnetic long-range order have become an interesting field of research in recent years. Frustrated magnetic systems are one of the best candidates to bring about such phases, such as spin-ice materials or spin liquids [1–3]. In fact, frustrated magnetic models imply large degenerate classical ground states (GSs) that are very sensitive to perturbations, such as thermal or quantum fluctuations, spin-orbit interactions, spin-lattice couplings, and impurities, all of which might be present in actual materials [4,5]. Novel unconventional phases, such as valence bond solids (VBSs) and spin liquids can emerge from the effect of such perturbations on classical frustrated systems. Moreover, the existence of artificial square ice [6–8] and the realization of quantum spin ice with Rydberg atoms [9] demand a comprehensive understanding of the associated models that are generic for such materials.

Generally, a spin system is frustrated whenever one cannot find a configuration of spins to fully satisfy the interacting bonds between every pair of spins [5,10]. For instance, a diagonal bond in addition to vertical and horizontal bonds construct a triangle, which makes frustration on the spins sitting on triangle corners of a square plaquette. In this respect, spin-1/2 antiferromagnetic Ising models on the $J_1 - J_2$ square and half depleted square, i.e., checkerboard, lattices are generic two-dimensional (2D) frustrated magnets in which J_1 and J_2, the strength of nearest- and next-nearest-neighbor interactions, respectively, compete with each other (see Fig. 1). These are prototype models that low dimensionality makes them an easier target for numerical/analytical approaches in contrast to three-dimensional counterparts [11–15]. Accordingly, the checkerboard lattice (CL) can be assumed as the 2D version of the pyrochlore lattice of true spin-ice materials [16]. Here, we focus particularly on the role of quantum fluctuations on the ground-state phase diagram of planar spin ice, namely, the CL and its low-energy effective theory on the square lattice (SL).

In the case of the Ising model on the CL, quantum fluctuations introduced by both the transverse magnetic field [16,17] and the in-plane XY interactions [18–21] lift the classical degeneracy of the highly frustrated point $J_2 = J_1$ toward a nonmagnetic plaquette-valence bond solid (-VBS) phase [16–18,22] with broken translational symmetry, which shows twofold degeneracy. The plaquette-VBS phase, which is mediated by anharmonic quantum fluctuations as an order-by-disorder phenomenon [23–25], emerges from an exponentially degenerate classical background, which cannot be observed within linear spin-wave theory [26,27] due to strong frustration. In order to shed more light on the highly frustrated region, in the first part of our paper, we obtain the GS phase diagram of the CL accurately by using a variational tree tensor network (TTN) ansatz and compare it with previous studies. We use a novel unconstrained (gauge-free) TTN, generalized to the CL to approximate the ground state of the system with higher accuracy compared with previous isometric schemes [28]. By computing local correlations and plaquette operator expectations, we find that a plaquette-VBS state is established

*langari@sharif.edu

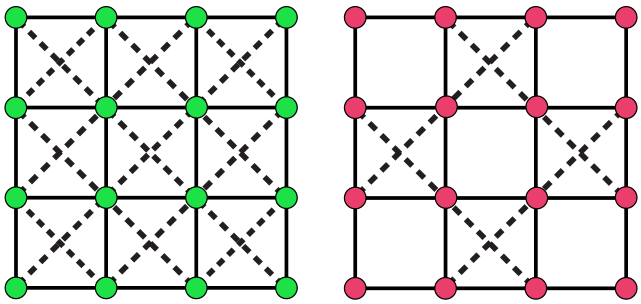

FIG. 1. $J_1 - J_2$ model on the (left) square lattice and the (right) checkerboard lattice. The solid and dashed lines are J_1 and J_2 bonds, respectively.

at the low magnetic field around the $J_2 = J_1$ region of the CL. Our results show that by increasing the transverse magnetic field, a second-order phase transition occurs at $\Gamma_c = 0.28$ from the plaquette-VBS phase to the paramagnetic phase. The associated critical exponents are $\nu = 1$ and $\gamma \simeq 0.4$, where ν reveals the divergence of correlation length and γ is an exponent, which governs the singularity in magnetic susceptibility. We do not observe any other critical point except the mentioned one, which rules out a canted Néel phase predicted by the Monte Carlo study [25] at $J_2 = J_1$. Our results of unconstrained TTN are in good agreement with the results of the cluster operator approach (COA) [22].

On the other hand, the $J_1 - J_2$ transverse-field Ising (TFI) model on the square lattice shows an emergent string-VBS phase at the fully frustrated point $J_2 = 0.5J_1$ [29,30]. It can be expressed that quantum fluctuations by means of a transverse field, lift the classical degeneracy toward doubly degenerate VBS states along the horizontal or vertical directions of the square lattice called the string-VBS phase. However, there is a possibility that such a phase can be extended to an intermediate region around the highly frustrated point $J_2 = 0.5J_1$, which is sandwiched between Néel and striped antiferromagnetic states for small and large J_2/J_1, respectively [31]. Accordingly, in the second part of our paper, we consider a different strategy to clarify the quantum phase diagram of the TFI model on the $J_1 - J_2$ SL. We introduce a mapping from the CL to the SL, which leads to the GS phase diagram of the $J_1 - J_2$ SL in terms of the phase diagram of the CL of the corresponding model. In other words, we claim that the low-energy effective theory of the frustrated TFI on the CL is given by the frustrated TFI on the SL. This mapping suggests a string-VBS order at the highly frustrated regime of the SL, which is in agreement with the results of the COA [29]. It is worth mentioning that the TFI model could represent the large easy-axis anisotropic limit of the antiferromagnetic $J_1 - J_2$ Heisenberg model where the true nature of a nonmagnetic (VBS) phase is still under debate on the SL [32–39] . Our results would be useful for further investigations in the latter model.

The paper is organized as follows. In the next section, we briefly introduce the model and different phases on the CL. In Sec. III, we inaugurate a numerical TTN technique to find accurately the quantum phase diagram of the CL. Then, in Sec. IV, we establish the mapping from the CL to the SL and

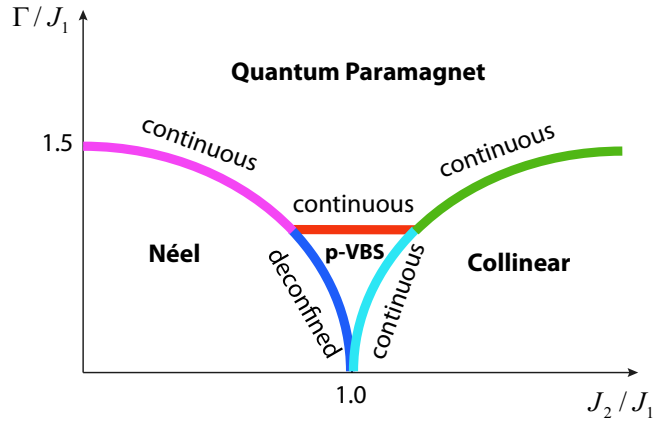

FIG. 2. A schematic phase diagram of the $S = 1/2$ $J_1 - J_2$ TFI model on the CL [22], including the information on the type of transitions between different phases obtained within TTN numerical simulation, namely, continuous and deconfined phase transitions.

derive the corresponding quantum phase diagram of the SL. Finally, the paper is summarized and concluded in Sec. V. The details of introduced mapping have been presented in the Appendix.

II. THE MODEL HAMILTONIAN

The Hamiltonian of the $J_1 - J_2$ transverse-field Ising model on the CL is as follows:

$$\mathcal{H} = J_1 \sum_{\langle i,j \rangle} S_i^z S_j^z + J_2 \sum_{\langle\langle i,j \rangle\rangle} S_i^z S_j^z - \Gamma \sum_i S_i^x, \qquad (1)$$

where $\langle i, j \rangle$ spans the nearest-neighbor sites with J_1 coupling, $J_2 > 0$ is the diagonal coupling on crossed plaquettes, Γ is the strength of transverse magnetic field, and $S^{x,z}$ refer to x and z components of spin-1/2 operators on the vertices of the lattice (see Fig. 1). It consists of four different phases, Néel and collinear ordered phases close to the nonfrustrated points $J_2/J_1 = 0$ and $J_2/J_1 = 2$, respectively, a quantum paramagnet phase at high fields, and a plaquette-VBS phase for low magnetic-fields $\Gamma \lesssim 0.3$, a narrow region around the highly frustrated point $J_2 = J_1$. The corresponding phase diagram is presented in Fig. 2, which has been obtained by the COA approach [22]. In fact, it has been concluded that the exponential degeneracy of the classical ground state at the highly frustrated point $J_2 = J_1$ (known as square ice [26]) is lifted toward a unique quantum plaquette-VBS state that breaks translational symmetry of the lattice with twofold degeneracy. It is a manifestation of order-by-disorder phenomena [23–25], which is induced by quantum fluctuations.

In the next section, we use the unconstrained TTN approach to further confirm the quantum GS phase diagram of the $J_1 - J_2$ TFI model on the CL. It has to be mentioned that the plaquette-VBS exists in a narrow region on the highly frustrated regime, which requires to be investigated within high accurate numerical simulations. In addition, we apply the TTN to find critical points and critical exponents of the phase transitions from the plaquette-VBS state to the Néel, collinear, and paramagnet phases, which can classify the type of phase transition.

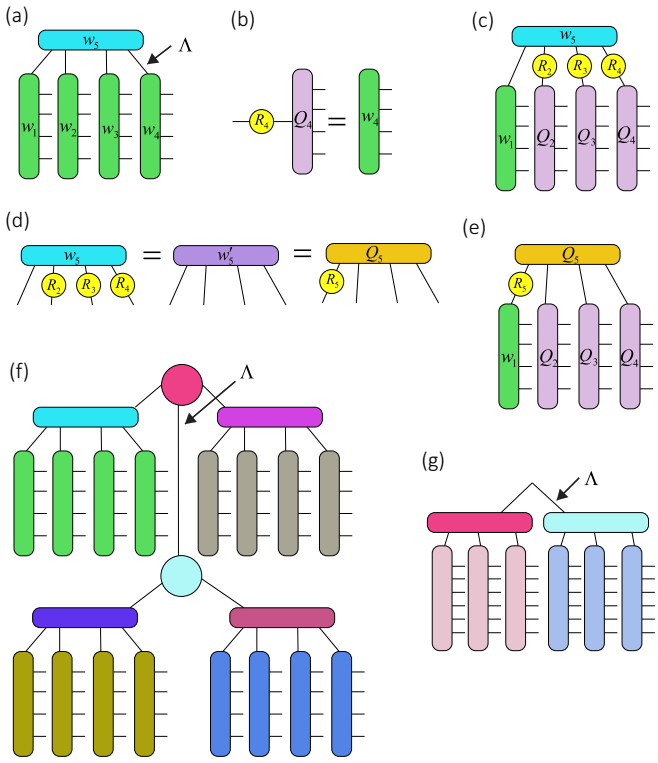

FIG. 3. Tensor network representation of an unconstrained TTN state $|\Psi\rangle$ and its canonical form. (a) A TTN state for a 4×4 square lattice is represented by tensors $\{w_i\}$ connected by the so-called virtual bonds with dimension Λ to form a treelike geometrical graph. (b) A tensor network representation of QR decomposition applied to tensor $w_4 = Q_4 R_4$. One needs to fuse lower indices and then represents it in a matrix form to perform decomposition. (c)–(e) The procedure to transform a general TTN state to a canonical normal form by using a sequence of QR decomposition. The norm tensor is defined by removing tensor w_1 from the tensor network representation of $\langle\Psi_{w_1}|\Psi_{w_1}\rangle$, denoted by $\mathcal{N}$. A sequence of QR decomposition is used to make norm tensor identity $\mathcal{N} = I$: tensors w_2, w_3, w_4 are decomposed into QR forms, and (d) then tensors R_2, R_3, R_4 are absorbed into tensor w_5, followed by a QR decomposition by fusing the virtual bonds (last ones) $w_5' = Q_5 R_5$. (e) The canonical procedure is completed by absorbing R_5 into w_1, i.e., $w_1' = w_1 R_5$. In this canonical form, one observes that $\langle\Psi|\Psi\rangle = \langle w_1'|I|w_1'\rangle$, i.e., the norm tensor is identity $\mathcal{N} = I$. The final optimum tensor w_1' is obtained by solving $H_{eff}|w_1'\rangle = \lambda_{\min}|w_1'\rangle$, where H_{eff} are obtained by removing tensor w_1' from $\langle\Psi_{w_1'}|H|\Psi_{w_1'}\rangle$.

III. UNCONSTRAINED TREE TENSOR NETWORK ANSATZ

The TTN states provide a variational ansatz [28,40–43] to simulate large 2D lattice sizes, beyond the possible sizes, which can be reached by exact diagonalization. We use an unconstrained TTN ansatz to variationally approximate the ground-state wave function of the TFI model Eq. (1) on the CL. The wave function is made of the local tensors $\{w_i\}$ connected to each other to form a treelike graph as shown in Fig. 3(a). The tensors $\{w_i\}$ effectively map a number of spins to an effective superspin by dimension Λ at each layer, making a coarse-graining transformation—each tensor w_i defines a projection from the original (physical) Hilbert space onto the relevant subspace. That is the basic idea in the renormalization group methodology invented by Kadanoff [44]. Here, the goal is to use an efficient variational ansatz to minimize the ground-state energy with respect to tensors $\{w_i\}$, finding the best variational parameters [which grows, such as $O(\Lambda^3)$]. In this paper, we use a recently introduced novel ansatz [43] which, in contrast to traditional schemes, releases the internal gauge symmetry of the tensors (the isometry constraint) and provides a computationally stable and efficient algorithm with higher accuracy.

We shortly explain the unconstrained TTN variational ansatz generalized to two-dimensional lattices. The optimization method is performed by minimizing the energy with respect to a specific tensor w_i (whereas holding fixed other tensors), i.e.,

$$\min_{w_i}\{\langle\Psi_{w_i}|H|\Psi_{w_i}\rangle - \lambda\langle\Psi_{w_i}|\Psi_{w_i}\rangle = \langle w_i|H_{\text{eff}}|w_i\rangle - \lambda\langle w_i|\mathcal{N}|w_i\rangle\},$$

where the so-called norm tensor $\mathcal{N}$ and effective Hamiltonian H_{eff} are obtained by removing tensor w_i from the tensor network representation of $\langle\Psi_{w_i}|\Psi_{w_i}\rangle$ and $\langle\Psi_{w_i}|H|\Psi_{w_i}\rangle$. The solution is given by solving a generalized eigenvalue problem $H_{\text{eff}}|w_i\rangle = \lambda_{\min}\mathcal{N}|w_i\rangle$, which is a standard equation in linear algebra. The optimization procedure is then completed by using an iterative strategy: At each step, only one tensor is optimized whereas others hold fixed, and then this task is repeated over all tensors until the variational energy does not change significantly. In practice, the norm tensor $\mathcal{N}$ causes instability in the algorithm, whereas the condition number (i.e., smallest singular value) would be too small. In order to avoid that, we need to use a "canonical normal form" [45] for the TTN state $|\Psi_{w_i}\rangle$ by making the norm tensor identity $\mathcal{N} = I$ (which is the best conditioning). The basic idea to do that is to use appropriate gauge transformations similar to the case of matrix product states: It is obtained by using a sequence of QR decomposition by fusing virtual bonds in a specific direction as shown in Figs. 3(b)–3(d). In this figure, we have explained how to use QR decomposition to end up with a canonical form. Once we obtain that, we replace the tensor w_i by solving the standard eigenvalue problem $H_{\text{eff}}|w_i\rangle = \lambda_{\min}|w_i\rangle$, which could be efficiently solved without suffering from bad conditioning.

The essential parameter Λ controls the accuracy of the TTN ansatz as for $\Lambda \to \infty$ the TTN state faithfully represents the actual ground state of the system. The computational cost of the algorithm scales, such as $O(\Lambda^4)$ and $O(\Lambda^3)$ for running time and memory, respectively. In the present numerical TTN simulation, we consider clusters 4×4, 6×6, and 8×8 with both periodic and open boundary conditions. We always perform a finite-size analysis to study the behavior of the order parameters. A polynomial fit up to the fourth order is used to extrapolate the expectation values in the $\Lambda \to \infty$ limit. The largest bond dimension that we could afford is $\Lambda \sim 500$ so that the error in the variational ground-state energy is, at least, on the order of 10^{-4} (near the critical point, which is the less accurate case).

$J_1 - J_2$ TFI model on the checkerboard lattice: TTN results

Before presenting the results, let us mention that the interesting and controversial part of the TFI model on the CL is in the low magnetic-field limit around the highly frustrated coupling $J_2 = J_1$. This clarifies the reason that we concentrate on this region, whereas the other parts of the phase diagram are known by other methods without doubt [22,26]. To obtain an accurate phase diagram for the $J_1 - J_2$ TFI model on the CL via the TTN approach, we compute the first and second derivatives of the ground-state energy by TTN simulation in two distinct directions on the phase diagram. First, we trace the phase diagram along Γ/J_1 at fixed $J_2 = J_1$, and then we consider another direction along J_2/J_1 at fixed magnetic-field $\Gamma/J_1 = cte$.

1. $J_2 = J_1$

According to the following equations, the first and second derivatives of the ground-state energy with respect to Γ for the limit $J_2 = J_1$ are equivalent to the transverse magnetization and magnetic susceptibility, respectively,

$$m_x = -\partial\langle\mathcal{H}\rangle/\partial\Gamma, \tag{2}$$

$$\chi = \partial m_x/\partial\Gamma = -\partial^2\mathcal{H}/\partial\Gamma^2. \tag{3}$$

Figures 4(a) and 4(b) show these quantities versus Γ/J_1 (at $J_2 = J_1$) obtained from TTN data for different lattice sizes. The transverse magnetization continuously reaches its saturated value, which rules out any first-order transition at this isotropic regime. However, we can see a peak on the magnetic susceptibility, which becomes sharper and stronger by increasing the lattice size, corresponding to a continuous second-order phase transition. We use finite-size scaling theory to evaluate the critical point and critical exponents for this transition [46]. The scaling behavior of χ, which governs the singularity at the critical point is

$$|\Gamma_c - \Gamma_{\max}| \sim N^{-1/2\nu}, \tag{4}$$

$$\chi(\Gamma_{\max}) \sim N^{\gamma/2\nu}, \tag{5}$$

where Γ_c is the critical field in the infinite size, $\Gamma_{\max}$ is the position of the extremum of finite-lattice susceptibility, ν is the correlation length exponent, i.e., $\xi \sim |\Gamma - \Gamma_c|^{-\nu}$, and γ exhibits the trend of singularity in the magnetic susceptibility.

We found a good scaling of TTN data, which give the critical field to be $\Gamma_c = 0.28 \pm 0.01$ in the thermodynamic limit. Interestingly, Fig. 5 confirms that both open and periodic boundary conditions lead to the same critical field $\Gamma_c \simeq 0.28$. This critical point is also in good accord with $\Gamma_c \simeq 0.3$ obtained from the COA results [22]. The inset of Fig. 4(b) shows the correlation length exponent obtained from finite-size scaling to be $\nu = 1.0 \pm 0.01$. Moreover, the scale-invariant behavior of magnetic susceptibility is shown in Fig. 4(c) representing a good data collapse of different sizes with exponent $\gamma = 0.44 \pm 0.01$. Furthermore, the presence of only one peak in magnetic susceptibility assures that two distinct phases exist at $J_2 = J_1$, which are separated at Γ_c. This single peak can be a signature for a quantum continuous phase transition from the plaquette-VBS phase at low fields to the quantum paramagnetic phase of high fields. The continuous nature of such a transition is also confirmed by the broken

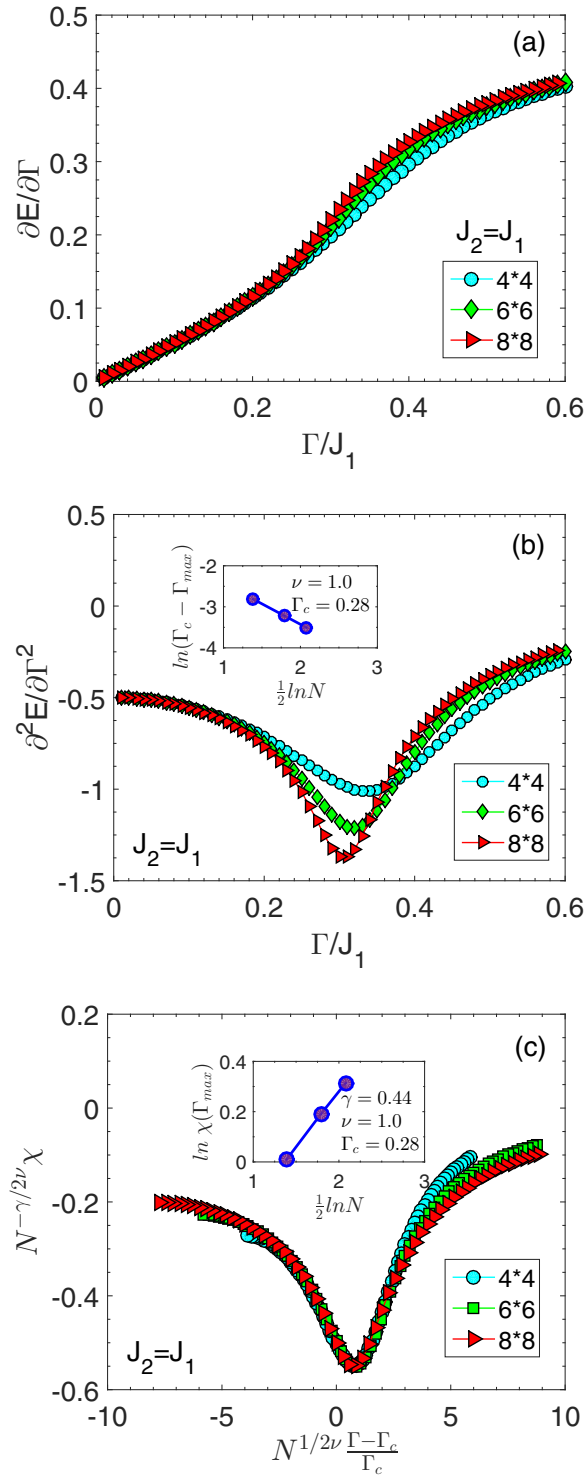

FIG. 4. (a) The first derivative of the GS energy with respect to Γ corresponding to the transverse magnetization obtained from TTN data for different system sizes. (b) The second derivative of the GS energy with respect to Γ, which is the magnetic susceptibility obtained from TTN simulation for different lattice sizes. It shows only a sharp peak indicating a phase transition from the plaquette-VBS phase in low fields to the quantum paramagnet phase in high fields at $(\Gamma/J_1)_c = 0.28 \pm 0.01$ with exponent $\nu = 1.0 \pm 0.01$. (c) Data collapse of magnetic susceptibility obtained from TTN data, which show the scale invariance of susceptibility governed by exponent $\gamma = 0.44 \pm 0.01$.

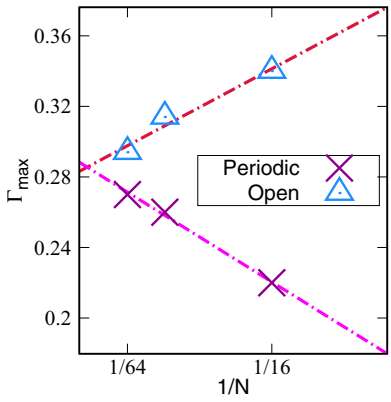

FIG. 5. The value of critical point versus inverse of lattice sizes. Both periodic and open boundary conditions are presented, which are fitted by the scaling relation $\Gamma(N) = \Gamma_c(\infty) + \frac{a}{N}$. We obtain $\Gamma_c(\infty) = 0.28 \pm 0.01$ and 0.285 ± 0.01 for open and periodic boundary conditions, respectively.

lattice translational symmetry of the plaquette-VBS phase compared with a symmetric quantum paramagnetic phase as we expect from a Landau-Ginzburg paradigm. The TTN results presented on the large two-dimensional lattices $N = 4 \times 4$, 6×6, and 8×8 do not show any signature for another phase transition at $J_2 = J_1$, which rules out the existence of a Néel order within $0.13 \lesssim \Gamma \lesssim 0.28$ that has been reported by Monte Carlo simulation in Ref. [25].

In order to confirm the nature of the ground state at low fields, we calculate the nearest-neighbor correlation function $C_{NN} = \langle S_i^z S_j^z \rangle$ using TTN simulations on the 8×8 lattice at $J_2 = J_1$. We obtained this correlation function for two different low and high values of transverse-field Γ, shown in Fig. 6. Correlations for the low-field regime depict a value close to the maximum value of Néel-type ordering $C_{NN}^{\max} = -0.25$ on the bonds of empty plaquettes with no corner sharing, whereas correlations have very small values on the other plaquettes. This is a clear signature of the plaquette formation as a VBS state, which breaks lattice translational

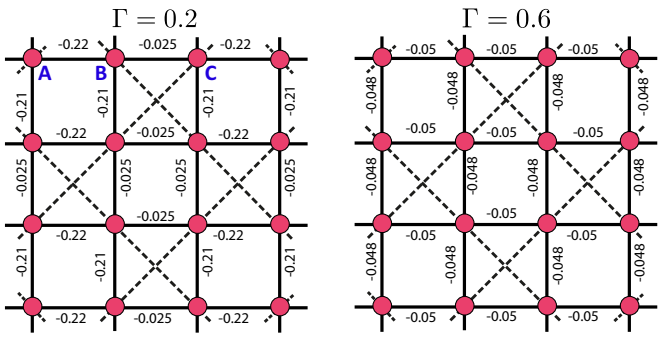

FIG. 6. Nearest-neighbor correlations, obtained by TTN numerical simulation on the center of a 8×8 lattice at the $J_2 = J_1$. Left: Correlations at $\Gamma/J_1 = 0.2$, which show the breaking of lattice translational symmetry corresponding to the plaquette-VBS phase. Right: Correlations at $\Gamma/J_1 = 0.6$ corresponding to the high-field regime of the quantum paramagentic phase, which preserves translational symmetry.

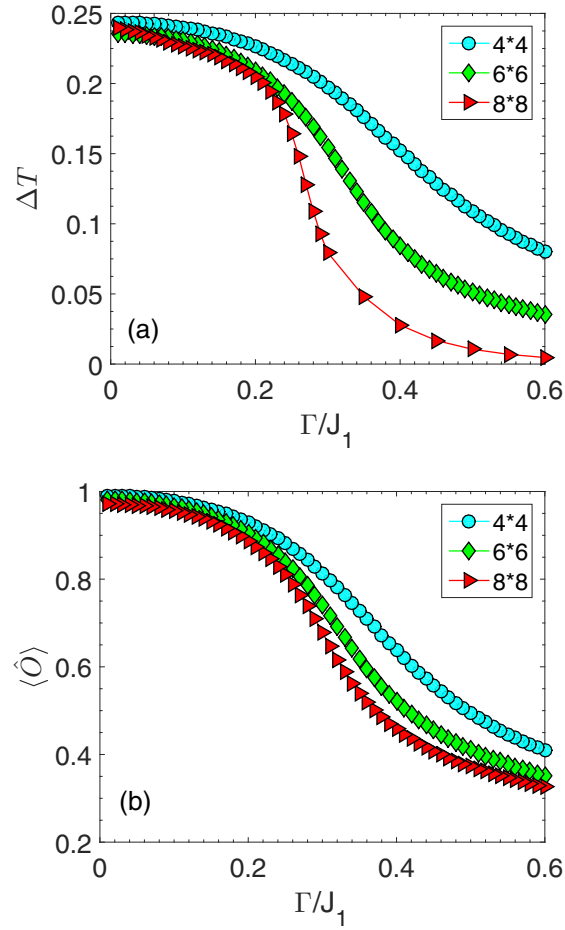

FIG. 7. (a) Expectation value of the translational order parameter ΔT and (b) the plaquette order parameter operator $\langle \hat{O} \rangle$ versus the transverse magnetic field, obtained by the unconstrained TTN ansatz on different lattice sizes.

symmetry leaving twofold degeneracy. However, by increasing the magnetic field to the high-field regime, we reach a quantum paramagnetic phase as it shows small correlations along vertical and horizontal directions of the lattice.

Moreover, we plot in Fig. 7(a), the translational order parameter, defined by

$$\Delta T = \langle S_A^z S_B^z \rangle - \langle S_B^z S_C^z \rangle, \tag{6}$$

as a function of Γ/J_1 for different system sizes where the sites A, B, and C are shown in Fig. 6. It is observed that by increasing system size the translational order parameter rapidly decreases (extrapolates to zero in the infinite-size limit) for $\Gamma > 0.3$ and tends to a finite value for $\Gamma < 0.3$ (lattice translational symmetry breaking), which is in agreement with the nature of the phases discussed above.

In addition, we support the plaquette-VBS nature of the ground state at low fields by calculating the ground-state expectation value of resonating plaquette operator ($\hat{O}$) [22,25]. This operator is defined as

$$\hat{O} = |\varphi\rangle\langle\bar{\varphi}| + |\bar{\varphi}\rangle\langle\varphi|, \tag{7}$$

where $|\varphi\rangle = |\uparrow\downarrow\uparrow\downarrow\rangle$ and $|\bar{\varphi}\rangle = |\downarrow\uparrow\downarrow\uparrow\rangle$ are two possible Néel configurations of a single plaquette. In fact, $\hat{O}$ defines

TABLE I. Numerical results of ground-state energy per site and plaquette order parameter obtained from TTN simulations on the 8 × 8 CL at $J_2 = J_1$ and open boundary conditions.

$J_2 = J_1$	$\Gamma = 0.1$	$\Gamma = 0.2$	$\Gamma = 0.3$	$\Gamma = 0.4$
E/N	−0.2525	−0.2607	−0.2770	−0.3050
$\langle\hat{o}\rangle$	0.9563	0.8866	0.6784	0.4579

a measure of resonating magnitude between $|\varphi\rangle$ and $|\bar{\varphi}\rangle$ on a plaquette. It is a suitable definition as it avoids formation of magnetic long-range orders, such as Néel and collinear states on the whole lattice. Hence, the expectation value of $\hat{O}$ is very close to one for a resonating plaquette-valence bond solid state, which has no magnetic order in the z direction. Figure 7(b) shows the expectation value of $\langle\hat{O}\rangle$ obtained by TTN simulation on different lattice sizes. It is evident that, for $J_2 = J_1$ and low fields, the value of $\langle\hat{O}\rangle$ is very close to unity which corresponds to the presence of a plaquette-VBS state.

2. $\Gamma/J_1 = 0.2$

To elucidate the structure of the phase diagram close to strong frustration, we fix the magnetic field in $\Gamma/J_1 = 0.2$ and trace the behavior along J_2/J_1. The first derivative of GS energy, according to relation $C^{(2)} = \langle S_i^z S_j^z\rangle_{\langle i,j\rangle} = \partial\langle\mathcal{H}\rangle/\partial J_2$, is equivalent to the next-nearest-neighbor spin-spin correlation. Figure 8(a) presents $C^{(2)}$ versus J_2/J_1, which shows a change in sign at $J_2 = J_1$. However, the derivative of $C^{(2)}$—that is the second derivative of energy—represents two peaks as shown in Fig. 8(b), which become sharper by increasing the lattice size. These peaks are interpreted as two critical points corresponding to two-phase transitions from the intermediate plaquette-VBS phase to the Néel and collinear phases on both sides of the phase diagram. The nature of quantum phase transition from the plaquette-VBS to Néel and collinear antiferromagnetic phases is an interesting feature of our results. The Néel and plaquette-VBS orders break different kinds of symmetries, i.e., Néel order breaks a discrete $Z2$ symmetry, whereas plaquette-VBS breaks lattice translational symmetry. We might expect that the nature of this transition is of the first-order type in terms of conventional Landau-Ginzburg theory. However, the first-order transition is ruled out by no singular behavior in the first derivative of the GS energy as shown in Fig. 8(a). Hence, we claim that the plaquette-VBS to Néel transition should be of a deconfined quantum continuous type according to the theory of deconfined quantum criticality [47]. The deconfined quantum critical point between Néel and plaquette-VBS phases occurs at $(J_2/J_1)_c = 0.9996$, which is completely consistent with the COA data reporting 0.999 [22]. On the other hand, as seen from Fig. 8, the plaquette-VBS to collinear phase transition is also continuous. However, it would be a conventional second-order phase transition, because both the plaquette-VBS and collinear phases break translational symmetry. The value of the latter critical point is $(J_2/J_1)_c = 1.0013$, which is also in agreement with the value of 1.001 obtained by the COA. The insets of Fig. 8(b) depict finite-size scaling data which reports the correlation length exponent to be $\nu \simeq 1.0$ for both transition points.

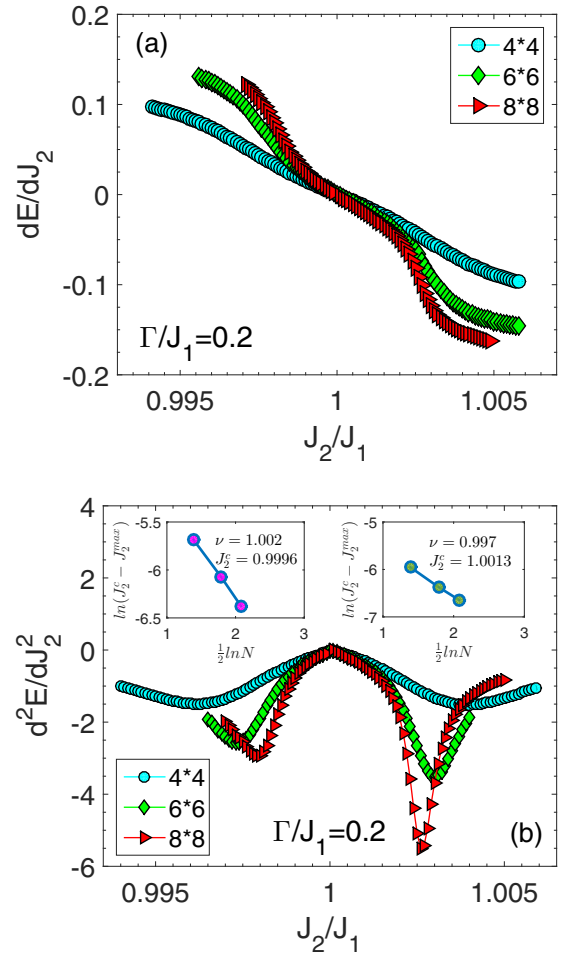

FIG. 8. (a) The first derivative of the GS energy with respect to J_2 at $\Gamma/J_1 = 0.2$, obtained from TTN simulation for different system sizes. (b) The second derivative of GS energy with respect to J_2 at $\Gamma/J_1 = 0.2$ shows two sharp peaks indicating phase transitions from the Néel and collinear phases to the intermediate plaquette-VBS phase. The critical points occur at $(J_2/J_1)_c = 0.9996 \pm 0.0001$ and $(J_2/J_1)_c = 1.0013 \pm 0.0001$, respectively, for Néel to plaquette-VBS and collinear to plaquette-VBS transitions, both with critical exponent $\nu \simeq 1.0$.

As a summary, Tables I and II show some numerical results obtained by TTN simulation. Table I represents numerical values of the ground-state energy and plaquette order parameter at $J_2 = J_1$ for different values of transverse-field Γ. In Table II, we tabulate the corresponding critical points and exponents obtained from finite-size scaling analysis on different parts of the phase diagram.

TABLE II. Numerical values of critical points and exponents resulting from the finite-size scaling analysis of TTN data for different regimes on the CL phase diagram.

$J_2 = J_1$			$\Gamma = 0.2,\ J_2 < J_1$		$\Gamma = 0.2,\ J_2 > J_1$	
Γ_c	ν	γ	J_{2c}	ν	J_{2c}	ν
0.28	1.0	0.44	0.9996	1.002	1.0013	0.997

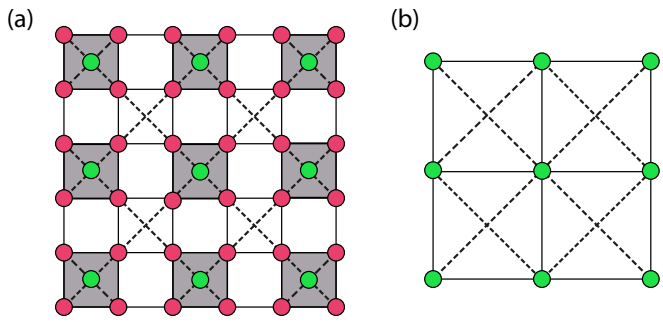

FIG. 9. Mapping from the CL to the square lattice. (a) Hatched crossed plaquettes of the CL form the unit cells of transformation. Solid and dashed lines are J_1 and J_2 bonds, respectively. Green bullets represent quasispins, which are associated with each unit cell. (b) A square lattice constructed from quasispins by a lattice spacing twice the original checkerboard one. Solid and dashed lines represent J_1 and J_2 bonds for the square lattice, respectively.

IV. MAP FROM THE CHECKERBOARD LATTICE TO THE SQUARE LATTICE

Here, we establish our map from the CL to the SL. Let us consider noncorner sharing set of crossed plaquettes on the CL, as unit cells of our transformation [see Fig. 9(a)]. According to Fig. 9(a), we assign a quasi-spin-half to each unit cell. These quasispins form a new square lattice, whose lattice spacing is twice that of the original lattice [see Fig. 9(b)]. Accordingly, the transverse-field Ising Hamiltonian Eq. (1) can be rewritten in the form

$$H = H_0 + H_{\rm int},$$
$$H_0 = \sum_I H_I, \quad H_{\rm int} = \sum_{\langle IJ\rangle} H_{IJ}, \tag{8}$$

where H_0 is the sum on the Hamiltonians of unit cells and $H_{\rm int}$ represents the interactions between unit cells. The Hamiltonian of a unit cell is diagonalized exactly, i.e., $J_1 - J_2$ TFI model on a crossed plaquette with four spins. Figure 10 shows the first four energy levels of a unit cell versus J_2/J_1 in an arbitrary transverse-field Γ. For $J_2 < J_1$, the first two eigenstates related to the lowest eigenenergies ϵ_1 and ϵ_2 are

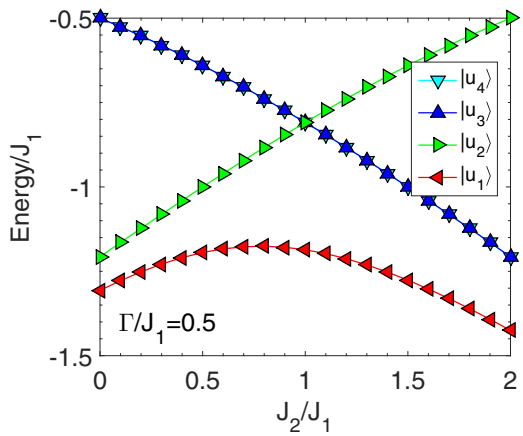

FIG. 10. The first four energy levels of a single crossed plaquette spectrum versus J_2/J_1 in (an arbitrary) transverse-field $\Gamma/J_1 = 0.5$.

$|u_1\rangle$ and $|u_2\rangle$, respectively. These eigenstates are considered as the bases for a quasispin ($\hat{\tau} = 1/2$) devoted to the unit cell. Hence, we define $|u_1\rangle_I = |\tau_I^z = \uparrow\rangle$ and $|u_2\rangle_I = |\tau_I^z = \downarrow\rangle$. On the other hand, for $J_2 > J_1$, the two eigenstates related to lowest eigenenergies are $|u_1\rangle$ and $|u_3\rangle$, where $|u_3\rangle$ is twofold degenerate, i.e., $\epsilon_3 = \epsilon_4$. Therefore, for $J_2 > J_1$, we consider two states $|u_1\rangle$ and $|u_2'\rangle = \frac{1}{\sqrt{2}}(|u_3\rangle + |u_4\rangle)$ as $|\uparrow\rangle$ and $|\downarrow\rangle$ quasispins, respectively.

In the next step, we define projection operators onto the subspace spanned by the low-energy sector of unit cells. In fact, the terminology of effective theory, which describes the low-energy behavior of a model is always accompanied by the reduction in the Hilbert space. We define two projection operators P_I and P_I' of the unit cell labeled by I for $J_2 < J_1$ and $J_2 > J_1$, respectively. They read as

$$P_I = |u_1\rangle_{II}\langle u_1| + |u_2\rangle_{II}\langle u_2|, \tag{9}$$
$$P_I' = |u_1\rangle_{II}\langle u_1| + |u_2'\rangle_{II}\langle u_2'|. \tag{10}$$

These local operators act as identity operators on other unit cells. Therefore, the projection operator for the whole lattice is defined as $P = \bigotimes_I P_I$ and $P' = \bigotimes_I P_I'$. Hence, the effective Hamiltonian in truncated subspace will be obtained from the following relations:

$$\mathcal{H}_{\rm eff} = P(\mathcal{H}_0 + \mathcal{H}_{\rm int})P \qquad (J_2 < J_1) \tag{11}$$
$$\mathcal{H}_{\rm eff} = P'(\mathcal{H}_0 + \mathcal{H}_{\rm int})P' \qquad (J_2 > J_1). \tag{12}$$

The explicit forms of $\mathcal{H}_0$ and $\mathcal{H}_{\rm int}$ in terms of original spin operators are given in Appendix.

The original Hamiltonian is renormalized in truncated subspace according to Eqs. (11) and (12), which leads to the effective Hamiltonian as follows:

$$J_2 < J_1:$$
$$\mathcal{H}^{\rm eff} = -2\alpha^2 J_1 \sum_{\langle I,J\rangle} \tau_I^x \tau_J^x + \alpha^2 J_2 \sum_{\langle\langle I,J\rangle\rangle} \tau_I^x \tau_J^x - (\epsilon_2 - \epsilon_1) \sum_I \tau_I^z,$$
$$J_2 > J_1:$$
$$\mathcal{H}^{\rm eff} = -2\alpha'^2 J_1 \sum_{\langle I,J\rangle_v} \tau_I^x \tau_J^x + 2\alpha'^2 J_1 \sum_{\langle I,J\rangle_h} \tau_I^x \tau_J^x$$
$$- \alpha'^2 J_2 \sum_{\langle\langle I,J\rangle\rangle} \tau_I^x \tau_J^x - (\epsilon_3 - \epsilon_1) \sum_I \tau_I^z, \tag{13}$$

where $\langle I,J\rangle_h$ and $\langle I,J\rangle_v$ run over horizontal and vertical nearest-neighbor bonds on the effective square lattice. The coefficients α and α' are functions of J_1, J_2, and Γ (see the Appendix). Let us make a π rotation around the z axis on the spins of one of the sublattices of the bipartite square lattice defined in Eq. (13), which contracts the minus sign in the first term. Similarly, a π rotation around the z axis on the spins sitting on even (or odd) labeled horizontal lines change the minus signs of the first and third terms of Eq. (14). Hence, all Ising terms ($\tau_I^x \tau_J^x$) in Eqs. (13) and (14) have positive couplings. Now, it is clear from the sign of nearest- and next-nearest-neighbor interactions of the effective Hamiltonian that there are Néel and striped orders for $J_2 \ll J_1$ and $J_2 \gg J_1$ limits, respectively. They correspond to well-known classical magnetic ordered phases of the Ising model on the $J_1 - J_2$ square lattice [48]. Hence, we can merge the two effective

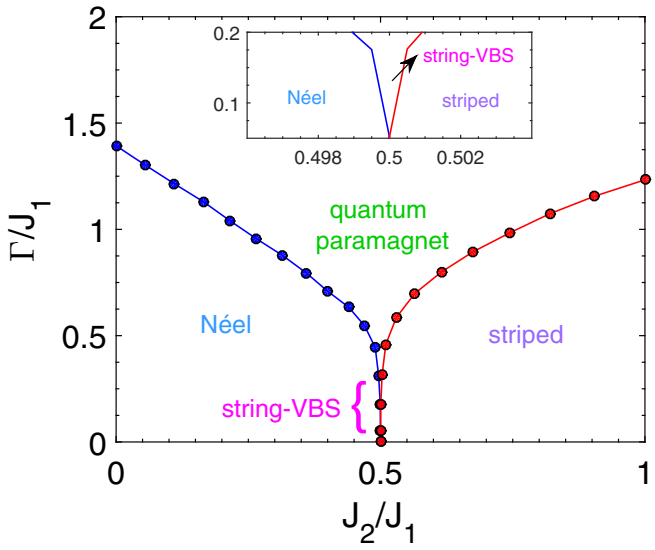

FIG. 11. Quantum GS phase diagram of the $J_1 - J_2$ TFI model on the square lattice obtained from the phase diagram of the CL [22] using the introduced effective theory. The inset indicates an opening of a narrow region of the string-VBS phase, which fills the space between the Néel and the striped phases around $J_2/J_1 = 0.5$ for low fields.

Hamiltonians (13) and (14) and write a unified effective Hamiltonian in terms of the renormalized parameters $\tilde{J}_1 - \tilde{J}_2$ that is a transverse-field Ising model on the effective square lattice,

$$\mathcal{H}^{\text{eff}} = \tilde{J}_1 \sum_{\langle I,J\rangle} \tau_I^x \tau_J^x + \tilde{J}_2 \sum_{\langle\langle I,J\rangle\rangle} \tau_I^x \tau_J^x - \tilde{\Gamma} \sum_I \tau_I^z, \qquad (14)$$

where

$$\begin{aligned} \frac{\tilde{J}_2}{\tilde{J}_1} &= \frac{1}{2}\frac{J_2}{J_1}, \\ \frac{\tilde{\Gamma}}{\tilde{J}_1} &= \frac{\epsilon_2 - \epsilon_1}{2\alpha^2 J_1} \qquad (J_2 < J_1), \\ \frac{\tilde{\Gamma}}{\tilde{J}_1} &= \frac{\epsilon_3 - \epsilon_1}{2\alpha'^2 J_1} \qquad (J_2 > J_1). \end{aligned} \qquad (15)$$

According to Eq. (14), the low-energy effective theory of the TFI model on the CL is provided with the same model on a square lattice with renormalized parameters given in Eq. (15). The effective Hamiltonian clearly shows that at the zero-field limit, the critical point $J_2 = J_1$ of the CL is mapped to the critical point $\tilde{J}_2 = 0.5\tilde{J}_1$ of the SL [see Eq. (15)]. Hence, the critical phase boundaries of the $\tilde{J}_1 - \tilde{J}_2$ TFI model on the SL can be achieved from the critical phase boundaries of the $J_1 - J_2$ TFI model on the CL.

GS phase diagram of the $J_1 - J_2$ TFI model on the square lattice

We implement the mapping established in the previous section and apply it to the GS phase diagram of the TFI model on the CL—which has been obtained by the COA [22]—to get the GS phase diagram of the $J_1 - J_2$ TFI model on the SL. To this end, we insert the location of critical boundaries of the CL phase diagram in Eqs. (15) to obtain the corresponding critical boundaries of the SL phase diagram. The outcome of this map is shown in Fig. 11. For instance, the critical point $\Gamma_c/J_1 = 0.3$ at $J_2 = J_1$ on the CL is mapped to $\Gamma_c/J_1 = 0.32$ at $J_2 = 0.5J_1$ on the SL. This result is consistent with the result $\Gamma_c/J_1 = 0.51$ obtained from TTN and COA data on the square lattice [29]. Moreover, Fig. 11 demonstrates the presence of a narrow region around $J_2 = 0.5J_1$ at low fields, exactly the same as what appeared in the phase diagram of the CL around the highly frustrated point $J_2 = J_1$ at low fields, such as Fig. 2. Hence, it can be deduced that quantum fluctuations of the weak transverse magnetic field induce a novel quantum state from the highly degenerate classical GS of the SL at $J_2 = 0.5J_1$, before reaching the quantum paramagnet phase at high fields.

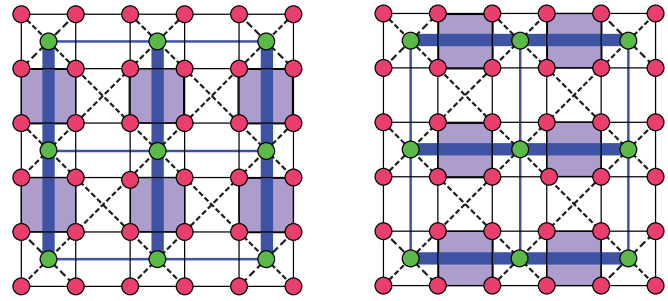

FIG. 12. Plaquette-VBS phase of the CL with broken translational symmetry with twofold degeneracy, which is mapped to the string-VBS phase of the square lattice with broken rotational symmetry and twofold degeneracy.

One of the smart features of the introduced mapping is to determine the structure of the novel state according to the plaquette-VBS state on the CL. Let us suppose that the CL is in the plaquette-VBS phase as shown by the color plaquettes in Fig. 12. In fact, each color plaquette is surrounded by two close sites on the effective square lattice. Therefore, whenever color plaquettes of the CL resonate between two possible Néel states, which comes from the nature of the plaquette-VBS phase, then they bring about a resonant situation on a set of sites on the effective square lattice resembling the string formation. Moreover, as the plaquette-VBS state of the CL breaks the translational symmetry of the lattice bearing twofold degeneracy, the emergence of strings on the effective SL could be either in vertical or horizontal directions, breaking the rotational symmetry of the lattice, which manifests the twofold degeneracy of string formations. This is in agreement with our earlier results in Ref. [29], which states that the highly degenerate classical ground state of the $J_1 - J_2$ TFI model on the SL at $J_2 = 0.5J_1$ goes to a unique string-VBS phase, when taking into account quantum fluctuations. This justifies the mapping procedure introduced here.

V. SUMMARY AND CONCLUSIONS

The transverse-field Ising model on two-dimensional checkerboard/square lattices would be a generic Hamiltonian to represent uniaxial magnets driven by quantum fluctuations.

It includes planar spin ice [16], artificial square ice [6–8], and even the realization of quantum spin ice with Rydberg atoms [9] that offer the emergence of novel phases. We have investigated the phase diagram of the $J_1 - J_2$ TFI model on a checkerboard lattice by an improved tree tensor network algorithm. We developed an unconstrained (gauge-free) tree tensor network ansatz, adapted to two-dimensional systems up to the lattice size 8×8 by relaxing the isometry constraint. At the highly frustrated point $J_2 = J_1$, we confirm a plaquette-VBS phase at low fields, separated from a paramagnet phase at $\Gamma_c \sim 0.28$. Utilizing finite-size scaling analysis on $N = 4 \times 4$, 6×6, and 8×8 lattices, we obtain the associated critical exponents to be $\nu \simeq 1$ and $\gamma \simeq 0.44$. We did not observe a signature of a canted Néel phase predicted by the Monte Carlo study [25], which is in agreement with previous results based on the cluster operator approach [22]. In addition, we found the nature and associated critical exponents of the quantum phase transitions from the plaquette-VBS phase to the adjacent Néel and collinear antiferromagnetic phases and to the quantum paramagnetic phase of high fields, summarized in Table II. It is shown that all transitions are of the second-order type except the transition from Néel to plaquette-VBS, which is of deconfined type, where the first derivative of ground-state energy indicates no singularity. However, we are not able to report a reasonable exponent for the fall off in correlation functions [49–53] due to finite lattice sizes ($\leqslant 8$) in our simulation. The schematic structure of the phase diagram is given in Fig. 2.

Our study justifies the importance of an unconstrained TTN ansatz as a promising numerical tool to address such highly frustrated systems where quantum Monte Carlo simulation fails due to the known sign problem for reaching ground-state properties. Furthermore, we have developed a mapping analysis to obtain quantum ground-state phase diagram of the $J_1 - J_2$ TFI model on the square lattice from the phase diagram of the $J_1 - J_2$ TFI model on the checkerboard lattice. An important outcome of our mapping is to clarify the VBS nature of the intermediate phase of the square-lattice phase diagram at low fields around the highly frustrated point $J_2 = 0.5J_1$. In fact, we showed that the plaquette-VBS phase of the checkerboard lattice is mapped to the string-VBS phase of the square lattice at the highly frustrated point $J_2 = 0.5J_1$, completely in agreement with the previous results of the $J_1 - J_2$ TFI model on the square lattice by the cluster operator approach, which describes such VBS ordering [29]. Briefly, we claim that the low-energy effective theory of the $J_1 - J_2$ TFI model on the checkerboard is given by the same model on the square lattice with renormalized parameters.

ACKNOWLEDGMENTS

A.L. would like to thank the Sharif University of Technology for financial support under Grant No. G960208. R.H. was supported by the Department of Energy, Office of Basic Energy Sciences, Division of Materials Sciences and Engineering, under Contract No. DE-AC02-76SF00515 through the SLAC National Accelerato Laboratory. We have used the UNI10 [54] library to build the TTN ansatz.

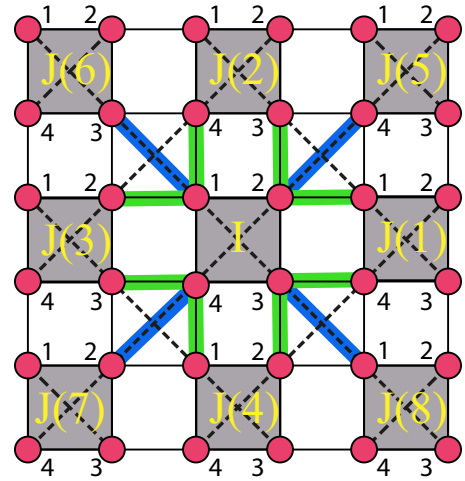

FIG. 13. The CL: each isolated plaquette I interacts with eight neighboring plaquettes. The green and blue lines, respectively, correspond to J_1 and J_2 interactions of plaquette I with its neighbors.

APPENDIX: MAPPING FROM THE CHECKERBOARD LATTICE TO THE SQUARE LATTICE

The details of the mapping procedure is presented here. As we explained in the text, if we divide the CL into non-corner-sharing crossed plaquettes, the transverse-field Ising Hamiltonian can be rewritten in the form $\mathcal{H} = \sum_I H_I + \sum_{\langle IJ \rangle} H_{IJ}$, where H_I is the Hamiltonian on a single plaquette and H_{IJ} defines the interaction Hamiltonian between single plaquettes. Figure 13 depicts a typical single plaquette I surrounded by eight independent plaquettes J interacting with it. According to site labeling of Fig. 13 we arrive at the following expression for H_I and H_{IJ}:

$$H_I = J_1\left(s^z_{1,I}s^z_{2,I} + s^z_{2,I}s^z_{3,I} + s^z_{3,I}s^z_{4,I} + s^z_{4,I}s^z_{1,I}\right) + J_2\left(s^z_{1,I}s^z_{3,I} + s^z_{2,I}s^z_{4,I}\right) - \Gamma\left(s^x_{1,I} + s^x_{2,I} + s^x_{3,I} + s^x_{4,I}\right), \tag{A1}$$

$$\begin{aligned} H_{IJ} = {} & J_1\left(s^z_{2,I}s^z_{1,J(1)} + s^z_{3,I}s^z_{4,J(1)}\right) + J_2\left(s^z_{2,I}s^z_{4,J(5)}\right) \\ & + J_1\left(s^z_{1,I}s^z_{4,J(2)} + s^z_{2,I}s^z_{3,J(2)}\right) + J_2\left(s^z_{1,I}s^z_{3,J(6)}\right) \\ & + J_1\left(s^z_{1,I}s^z_{2,J(3)} + s^z_{4,I}s^z_{3,J(3)}\right) + J_2\left(s^z_{4,I}s^z_{2,J(7)}\right) \\ & + J_1\left(s^z_{4,I}s^z_{1,J(4)} + s^z_{3,I}s^z_{2,J(4)}\right) + J_2\left(s^z_{3,I}s^z_{1,J(8)}\right). \end{aligned} \tag{A2}$$

Let us consider the case $J_1 > J_2$, we consider the first two eigenstates $|u_1\rangle$ and $|u_2\rangle$ of H_I—corresponding to the first two energy levels of it—as two components of new quasispins assigned to each single plaquette. Then, we define the projection operator P_0 as $P_0 = |u_1\rangle\langle u_1| + |u_2\rangle\langle u_2|$ to renormalize original spin operators in the truncated subspace according to the following equations:

$$\begin{aligned} & P_0 s^z_1 P_0 = P_0 s^z_3 P_0 = \alpha \tau^x_I, \\ & P_0 s^z_2 P_0 = P_0 s^z_4 P_0 = -\alpha \tau^x_I, \\ & P_0 s^x_1 P_0 = P_0 s^x_2 P_0 = P_0 s^x_3 P_0 = P_0 s^x_4 P_0 = (\beta - \gamma)\tau^z_I, \end{aligned} \tag{A3}$$

where $\alpha = 4A_2B_1 + 2A_4B_2$, $\beta = 2A_2(A_1 + 2A_3 + A_4)$, and $\gamma = 2B_1B_2$ in which the coefficients A, B are given by the

matrix elements of eigenvectors $|u_1\rangle$ and $|u_2\rangle$,

$$|u_1\rangle = \begin{pmatrix} A_1 \\ A_2 \\ A_2 \\ A_3 \\ A_2 \\ A_4 \\ A_3 \\ A_2 \\ A_2 \\ A_3 \\ A_4 \\ A_2 \\ A_3 \\ A_2 \\ A_2 \\ A_1 \end{pmatrix}, \qquad |u_2\rangle = \begin{pmatrix} 0 \\ B_1 \\ -B_1 \\ 0 \\ B_1 \\ B_2 \\ 0 \\ B_1 \\ -B_1 \\ 0 \\ -B_2 \\ -B_1 \\ 0 \\ B_1 \\ -B_1 \\ 0 \end{pmatrix}. \tag{A4}$$

These matrix elements are functions of J_1, J_2, and Γ, which are lengthy and complicated expressions. The simplest one is B_1, which has the following form:

$$B_1 = -\frac{2}{\sqrt{\frac{2[\sqrt{16\Gamma^2+(J_2-2J_1)^2}+2J_1-J_2]^2}{\Gamma^2}+32}}. \tag{A5}$$

Now, we rewrite the Hamiltonians H_I and H_{IJ} of Eqs. (A1) and (A2) in terms of new quasispins and finally obtain the effective Hamiltonian,

$$J_2 < J_1:$$
$$\mathcal{H}^{\text{eff}} = -2\alpha^2 J_1 \sum_{\langle I,J\rangle} \tau_I^x \tau_J^x + \alpha^2 J_2 \sum_{\langle\langle I,J\rangle\rangle} \tau_I^x \tau_J^x - (\epsilon_2 - \epsilon_1) \sum_I \tau_I^z, \tag{A6}$$

where ϵ_1 and ϵ_2 are eigenenergies of a single plaquette, corresponding to eigenvectors $|u_1\rangle$ and $|u_2\rangle$, respectively. We perform a π rotation on spins on only even (or odd) sites of the bipartite square lattice. It finally leads to an effective Hamiltonian for $J_2 < J_1$ as

$$\mathcal{H}^{\text{eff}} = J_1' \sum_{\langle I,J\rangle} \tau_I^x \tau_J^x + J_2' \sum_{\langle\langle I,J\rangle\rangle} \tau_I^x \tau_J^x - \Gamma' \sum_I \tau_I^z, \tag{A7}$$

where

$$\frac{J_2'}{J_1'} = \frac{1}{2}\frac{J_2}{J_1}, \qquad \frac{\Gamma'}{J_1'} = \frac{\epsilon_2 - \epsilon_1}{2\alpha^2} \qquad (J_2 < J_1). \tag{A8}$$

A similar procedure is also performed for the case $J_2 > J_1$.

[1] M. J. Harris, S. T. Bramwell, D. F. McMorrow, T. Zeiske, and K. W. Godfrey, Phys. Rev. Lett. **79**, 2554 (1997).
[2] S. T. Bramwell and M. J. P. Gingras, Science **294**, 1495 (2001).
[3] C. Nisoli, R. Moessner, and P. Schiffer, Rev. Mod. Phys. **85**, 1473 (2013).
[4] C. Lacroix, P. Mendels, and F. Mila, *Introduction to Frustrated Magnetism: Materials, Experiments, Theory* (Springer, Berlin, 2013).
[5] H. T. Diep, *Frustrated Spin Systems*, 2nd ed. (World Scientific, Singapore, 2013).
[6] R. F. Wang, C. Nisoli, R. S. Freitas, J. Li, W. McConville, B. J. Cooley, M. S. Lund, N. Samarth, C. Leighton, V. H. Crespi, and P. Schiffer, Nature (London) **439**, 303 (2006).
[7] R. Wang, J. Li, W. McConville, C. Nisoli, X. Ke, J. Freeland, V. Rose, M. Grimsditch, P. Lammert, V. Crespi *et al.*, J. Appl. Phys. **101**, 09J104 (2007).
[8] X. Ke, J. Li, C. Nisoli, P. E. Lammert, W. McConville, R. F. Wang, V. H. Crespi, and P. Schiffer, Phys. Rev. Lett. **101**, 037205 (2008).
[9] A. W. Glaetzle, M. Dalmonte, R. Nath, I. Rousochatzakis, R. Moessner, and P. Zoller, Phys. Rev. X **4**, 041037 (2014).
[10] R. Moessner, Can. J. Phys. **79**, 1283 (2001).
[11] R. Siddharthan, B. S. Shastry, A. P. Ramirez, A. Hayashi, R. J. Cava, and S. Rosenkranz, Phys. Rev. Lett. **83**, 1854 (1999).
[12] Y. K. Tsui, C. A. Burns, J. Snyder, and P. Schiffer, Phys. Rev. Lett. **82**, 3532 (1999).
[13] J. S. Gardner, S. R. Dunsiger, B. D. Gaulin, M. J. P. Gingras, J. E. Greedan, R. F. Kiefl, M. D. Lumsden, W. A. MacFarlane, N. P. Raju, J. E. Sonier, I. Swainson, and Z. Tun, Phys. Rev. Lett. **82**, 1012 (1999).
[14] R. G. Melko, B. C. den Hertog, and M. J. P. Gingras, Phys. Rev. Lett. **87**, 067203 (2001).
[15] J. P. C. Ruff, R. G. Melko, and M. J. P. Gingras, Phys. Rev. Lett. **95**, 097202 (2005).
[16] R. Moessner, O. Tchernyshyov, and S. L. Sondhi, J. Stat. Phys. **116**, 755 (2004).
[17] R. Moessner and S. L. Sondhi, Phys. Rev. B **63**, 224401 (2001).
[18] N. Shannon, G. Misguich, and K. Penc, Phys. Rev. B **69**, 220403(R) (2004).
[19] O. A. Starykh, A. Furusaki, and L. Balents, Phys. Rev. B **72**, 094416 (2005).
[20] Y.-H. Chan, Y.-J. Han, and L.-M. Duan, Phys. Rev. B **84**, 224407 (2011).
[21] R. F. Bishop, P. H. Y. Li, D. J. J. Farnell, J. Richter, and C. E. Campbell, Phys. Rev. B **85**, 205122 (2012).
[22] M. Sadrzadeh and A. Langari, Eur. Phys. J. B **88**, 259 (2015).
[23] J. Villain, R. Bidaux, J.-P. Carton, and R. Conte, J. Phys. **41**, 1263 (1980).
[24] L. Bellier-Castella, M. J. Gingras, P. C. Holdsworth, and R. Moessner, Can. J. Phys. **79**, 1365 (2001).
[25] L.-P. Henry and T. Roscilde, Phys. Rev. Lett. **113**, 027204 (2014).
[26] L.-P. Henry, P. C. W. Holdsworth, F. Mila, and T. Roscilde, Phys. Rev. B **85**, 134427 (2012).
[27] M. Sadrzadeh and A. Langari, J. Phys.: Conf. Ser. **969**, 012114 (2018).
[28] L. Tagliacozzo, G. Evenbly, and G. Vidal, Phys. Rev. B **80**, 235127 (2009).
[29] M. Sadrzadeh, R. Haghshenas, S. S. Jahromi, and A. Langari, Phys. Rev. B **94**, 214419 (2016).

[30] M. Sadrzadeh and A. Langari, Physica C **549**, 1 (2018).
[31] A. Kalz, A. Honecker, S. Fuchs, and T. Pruschke, J. Phys.: Conf. Ser. **145**, 012051 (2009).
[32] S. Sachdev and R. N. Bhatt, Phys. Rev. B **41**, 9323 (1990).
[33] M. E. Zhitomirsky and K. Ueda, Phys. Rev. B **54**, 9007 (1996).
[34] G.-M. Zhang, H. Hu, and L. Yu, Phys. Rev. Lett. **91**, 067201 (2003).
[35] L. Capriotti, F. Becca, A. Parola, and S. Sorella, Phys. Rev. B **67**, 212402 (2003).
[36] O. A. Starykh and L. Balents, Phys. Rev. Lett. **93**, 127202 (2004).
[37] M. Mambrini, A. Läuchli, D. Poilblanc, and F. Mila, Phys. Rev. B **74**, 144422 (2006).
[38] R. Haghshenas and D. N. Sheng, Phys. Rev. B **97**, 174408 (2018).
[39] R. Haghshenas, W.-W. Lan, S.-S. Gong, and D. N. Sheng, Phys. Rev. B **97**, 184436 (2018).
[40] Y.-Y. Shi, L.-M. Duan, and G. Vidal, Phys. Rev. A **74**, 022320 (2006).
[41] P. Silvi, V. Giovannetti, S. Montangero, M. Rizzi, J. I. Cirac, and R. Fazio, Phys. Rev. A **81**, 062335 (2010).
[42] V. Murg, F. Verstraete, O. Legeza, and R. M. Noack, Phys. Rev. B **82**, 205105 (2010).
[43] M. Gerster, P. Silvi, M. Rizzi, R. Fazio, T. Calarco, and S. Montangero, Phys. Rev. B **90**, 125154 (2014).
[44] E. Efrati, Z. Wang, A. Kolan, and L. P. Kadanoff, Rev. Mod. Phys. **86**, 647 (2014).
[45] F. Verstraete, V. Murg, and J. Cirac, Adv. Phys. **57**, 143 (2008).
[46] H. Nishimori and G. Ortiz, *Elements of Phase Transitions and Critical Phenomena* (Oxford University Press, Oxford, 2011).
[47] T. Senthil, A. Vishwanath, L. Balents, S. Sachdev, and M. P. A. Fisher, Science **303**, 1490 (2004).
[48] J. L. Morán-López, F. Aguilera-Granja, and J. M. Sanchez, Phys. Rev. B **48**, 3519 (1993).
[49] A. W. Sandvik, Phys. Rev. Lett. **98**, 227202 (2007).
[50] J. Lou, A. W. Sandvik, and N. Kawashima, Phys. Rev. B **80**, 180414(R) (2009).
[51] S. Pujari, K. Damle, and F. Alet, Phys. Rev. Lett. **111**, 087203 (2013).
[52] S. Pujari, F. Alet, and K. Damle, Phys. Rev. B **91**, 104411 (2015).
[53] L. Wang, Z.-C. Gu, F. Verstraete, and X.-G. Wen, Phys. Rev. B **94**, 075143 (2016).
[54] Y.-J. Kao, Y.-D. Hsieh, and P. Chen, J. Phys.: Conf. Ser. **640**, 012040 (2015).